

A cluster of outflows in the Vulpecula Rift

J. C. Mottram^{1*} and C. M. Brunt¹

¹*School of Physics, University of Exeter, Exeter, Devon, EX4 4QL, UK*

Accepted 2011 September 15. Received 2011 September 14; in original form 2011 June 16

ABSTRACT

We present ^{12}CO , ^{13}CO and C^{18}O ($J=3-2$) observations of a new cluster of outflows in the Vulpecula Rift with HARP-B on the JCMT. The mass associated with the outflows, measured using the ^{12}CO HARP-B observations and assuming a distance to the region of 2.3 kpc, is 129 M_{\odot} , while the mass associated with the dense gas from C^{18}O observations is 458 M_{\odot} and the associated sub-millimeter core has a mass of $327 \pm 112\text{ M}_{\odot}$ independently determined from Bolocam 1.1mm data. The outflow-to-core mass ratio is therefore ~ 0.4 , making this region one of the most efficient observed thus far with more than an order of magnitude more mass in the outflow than would be expected based on previous results. The kinetic energy associated with the flows, 94×10^{45} ergs, is enough to drive the turbulence in the local clump, and potentially unbind the local region altogether. The detection of SiO ($J=8-7$) emission toward the outflows indicates that the flow is still active, and not simply a fossil flow. We also model the SEDs of the four YSOs associated with the molecular material, finding them all to be of mid to early B spectral type. The energetic nature of the outflows and significant reservoir of cold dust detected in the sub-mm suggest that these intermediate mass YSOs will continue to accrete and become massive, rather than reach the main sequence at their current mass.

Key words: ISM: jets and outflows, stars: winds, outflows, molecular data, stars:formation, stars: pre-main-sequence

1 INTRODUCTION

Molecular outflows are observed towards stars of all masses during their formation (Arce et al. 2007), and are generally associated with both active accretion (see e.g. Churchwell 1999; Pudritz et al. 2007) and loss of angular momentum from the star/disk system that they originate from (e.g. Tomisaka 2000; Yamada et al. 2009). Early observations suggested that different scenarios for outflow generation might be required for the low and high mass regimes (see e.g. Richer et al. 2000, and references therein.). However, higher-resolution studies of massive outflows have shown that these differences were exaggerated by the low-resolution single-dish observations used and that their properties transition relatively smoothly as a function of mass (e.g. Beuther et al. 2002c,a).

In addition to being signposts of active star formation, the mass, energy and angular momentum transported by molecular outflows can also have a significant impact on the surrounding molecular clouds in which young stars form. This can be through the driving of turbulence within the cloud (e.g. Matzner 2007; Brunt, Heyer & Mac Low

2009), at least on small scales, or, for particularly powerful outflows, even contribute to the dispersal of the cloud and removal of the reservoir for further star formation (Matzner & McKee 2000). A recent study of the outflows in the Perseus molecular cloud by Curtis et al. (2010, see also Hatchell & Dunham 2009 and Arce et al. 2010) has shown that outflows can contribute a significant amount of energy to driving turbulence and cloud dispersal for whole molecular clouds, though they may not always be energetic enough to dominate these processes on their own. Recent investigations into how the energy and momentum transported by outflows is translated to the cloud (e.g. Banerjee, Klessen & Fendt 2007; Nakamura & Li 2007; Carroll et al. 2009) show efficiencies which can be strongly scale-dependent, so even if outflows in a given cloud are not powerful enough to disrupt the whole cloud complex, they may be significant on the intermediate cluster scales.

In this paper we present recent observations of a new outflow discovered at $\ell = 59.6375^\circ$, $b = -00.1875^\circ$ in the ^{12}CO ($J=1-0$) observations of the Exeter FCRAO (Five-College Radio Astronomical Observatory) CO Survey (Mottram & Brunt 2010, Brunt et al., 2011, in prep.), which have a spatial resolution of $45''$ and a velocity resolution of $\sim 0.15\text{ km s}^{-1}$. The systematic velocity of the cloud emission

* E-mail: joe@astro.ex.ac.uk

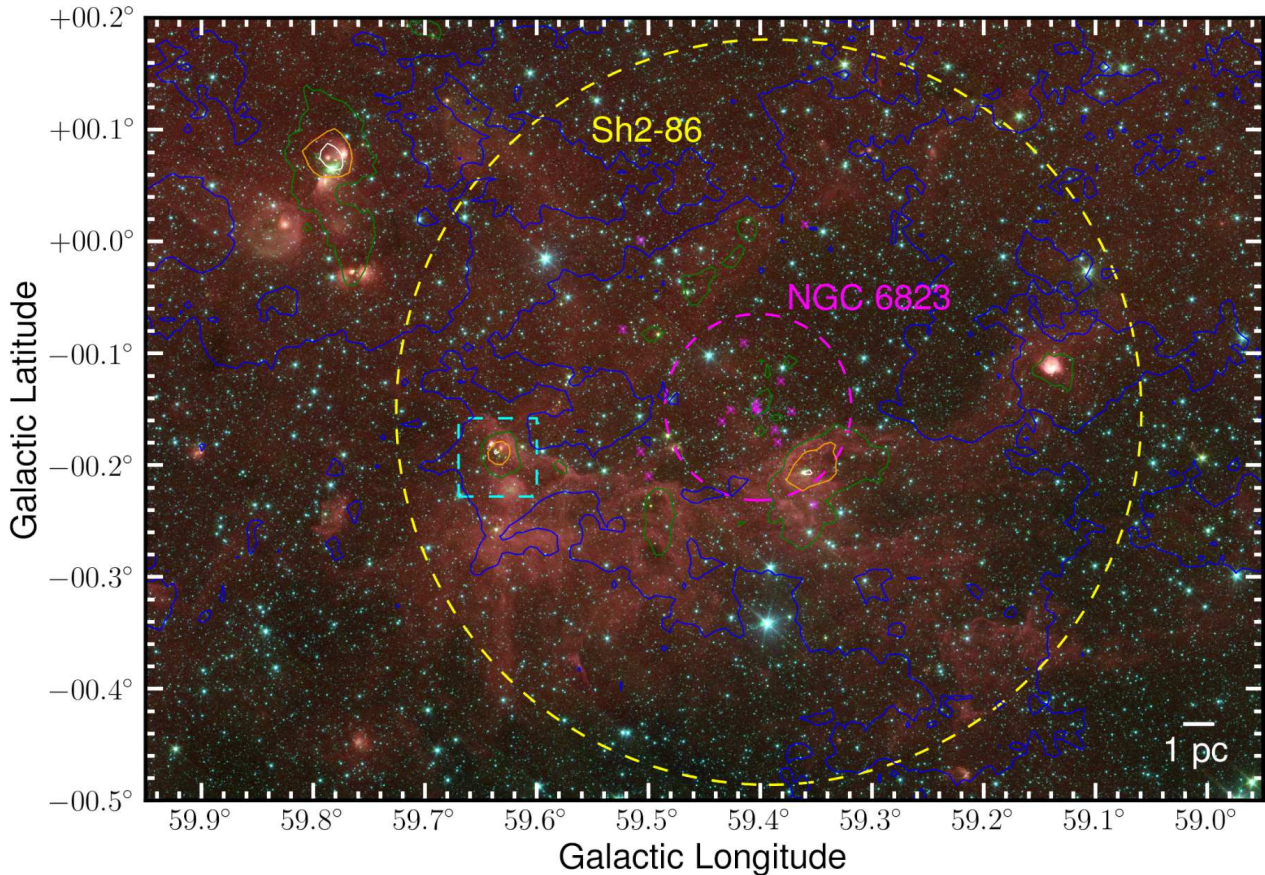


Figure 1. Infrared three-colour GLIMPSE (Benjamin et al. 2003) IRAC 3.6 μm (blue), 4.5 μm (green) and 8.0 μm (red) image of part of the Vulpecula Rift with overlaid contours showing integrated Exeter-FCRAO Survey (Mottram & Brunt 2010, Brunt et al., 2011, in prep.) ^{12}CO emission. The contour levels for the integrated emission are 25, 50, 75 and 100 K km s^{-1} , and are coloured blue, green, orange and white respectively. The cyan dashed square indicates the region around the newly discovered outflow which will be explored in this paper, while the yellow dashed circle indicates the original identification of the evolved H II region Sh2-86 by Sharpless (1959). The magenta crosses indicate the positions of the OB stars identified towards the cluster NGC6832 by Massey, Johnson & Degioia-Eastwood (1995), while the magenta dashed circle shows the approximate region containing the main cluster as identified by Bica, Bonatto & Dutra (2008).

associated with the outflow is $\sim 27.5 \text{ km s}^{-1}$, and the outflow is essentially unresolved in these data. A three-colour GLIMPSE (Benjamin et al. 2003) map, with contours showing the integrated FCRAO ^{12}CO ($J=1-0$) emission in the region and the outflow position marked is presented in Figure 1.

A sub-mm/mm core identified by Chapin et al. (2008) using BLAST (Pascale et al. 2008) at $\ell = 059.6331$, $b = -00.1906$ (their V52), who derive a core mass of $390 \pm 75 M_{\odot}$ and luminosity of $3850 \pm 610 L_{\odot}$, is associated with the outflow. The core is also detected in the Bolocam Galactic Plane Survey (BGPS Aguirre et al. 2011) at 1.1mm which, using the median gas temperature of 27 K (obtained during outflow property calculation in section 3), the source integrated flux and equation 10 from Rosolowsky et al. (2010), gives a core mass of $327 \pm 112 M_{\odot}$.

The outflow also lies near several mid/far-IR bright sources as shown in the three-colour combination GLIMPSE, MIPS GAL (Carey et al. 2009) and

Hi-GAL (Molinari et al. 2010b,a) images in Figure 2, which are part of the Vulpecula Rift molecular cloud complex. The region is near the large H II region Sh-86 (Sharpless 1959) and the young cluster NGC 6832 (Massey, Johnson & Degioia-Eastwood 1995, see Figure 1), part of the VulOB 1 OB association. There have been some suggestions that the whole region is undergoing sequential star formation (e.g. Ehlerová, Palouš & Huchtmeier 2001), but Billot et al. (2010) find no evidence for this in the YSO population as obtained from GLIMPSE and MIPS GAL observations. In terms of the early phases of star formation and evolution, Billot et al. (2011) found an increase in clustering of sources as wavelength decreases in the five Herschel bands (70 μm , 160 μm , 250 μm , 350 μm , 500 μm) of the Hi-GAL Science Demonstration Phase (SDP) observations of this region (Molinari et al. 2010a). While detailed identification of evolutionary phases has not been completed, this tentatively indicates that warmer sources are more likely to be in clusters within the region.

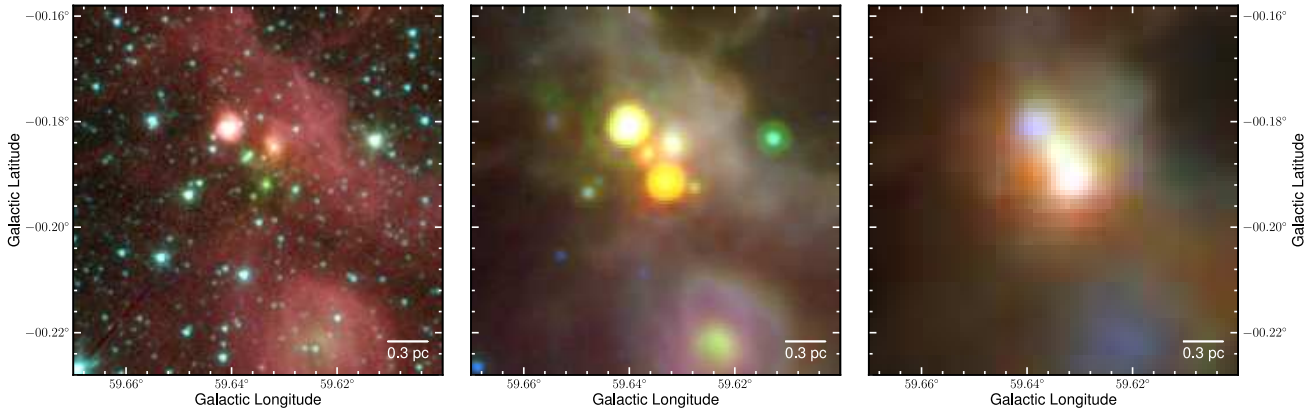


Figure 2. Infrared three-colour images of the region around the outflows. Left: GLIMPSE IRAC 3.6 μm (blue), 4.5 μm (green) and 8.0 μm (red). Centre: GLIMPSE IRAC 8.0 μm (blue), MIPS GAL (Carey et al. 2009) 24 μm (green) and Hi-GAL (Molinari et al. 2010b,a) PACS 70 μm (red). Right: Hi-GAL PACS 70 μm (blue), PACS 160 μm (green) and SPIRE 250 μm (red).

The molecular cloud properties of the whole Vulpecula Rift as observed in the Exeter FCRAO CO Survey will be discussed in an upcoming paper (Mottram *et al.*, in prep.).

The kinematic distance relating to the systematic outflow velocity, using the Brand & Blitz (1993) rotation curve, is 2.7 kpc if the source is at the near distance and 5.9 kpc if at the far distance. The outflow is most likely associated with the Vulpecula Rift molecular cloud complex, which infrared extinction maps suggest is at the near distance (e.g. Russeil et al. 2011). The open cluster NGC 6823 also lies within the cloud complex, for which Massey, Johnson & Degioia-Eastwood (1995) derive a photometric distance of 2.3 kpc. We therefore follow the approach of both Chapin et al. (2008) and Russeil et al. (2011) in assuming a distance of 2.3 kpc to the region.

It is perhaps surprising that an outflow associated with such a massive core has not been discovered sooner, but this might be because it only has an upper limit at 25 μm in the IRAS point source catalogue (PSC, Beichman et al. 1988) which would have caused it to be excluded from the selection criteria of previous studies (e.g. Beuther et al. 2002c, who used the sample of Sridharan et al. 2002).

We begin by describing the JCMT observations in section 2, after which we describe the method used to identify the outflow velocity windows and calculate outflow properties in section 3. In section 4 we present results and analysis of the outflow properties, as well as those relating to the local molecular material and the young stellar objects (YSOs) most probably associated with the outflow. Finally, we provide a short discussion of the wider context of our results and reach our conclusions in sect. 5.

2 JCMT OBSERVATIONS

Mapping observations of ^{12}CO , ^{13}CO and C^{18}O ($J=3-2$) and single pointing grid observations of HCO^+ , H^{13}CO^+ ($J=4-3$) and SiO ($J=8-7$) were obtained with HARP-B and the ACSIS autocorrelator (Buckle et al. 2009) at the James Clerk Maxwell Telescope (JCMT), Mauna Kea, Hawaii on the 1st and 3rd of November 2009 as service proposal S09BU01. The spatial resolution of the JCMT at the ob-

served frequencies is $\sim 14''$, with a main beam efficiency $\eta_{MB} = 0.61$ (Buckle et al. 2009). Though HARP-B consists of a 4×4 pixel array of receivers, four of these pixels (H00, H01, H02 and H14) were not operational at the time of observing. For each of the CO lines, four sets of observations in position-switching raster mode were undertaken with a quarter array shift ($29.1''$) between each scan. A 90° scan direction change was also implemented between each pair of observations, after which the array was offset by an eighth ($14.6''$) in both the x and y plane of the array and the process repeated. The resulting basket-woven maps cover an area of $4' \times 4'$ centred on G059.6331–00.1906 ($\alpha = 19^h 43^m 49.68^s$, $\delta = +23^\circ 28' 38.3''$ and $V_{LSR} = +25 \text{ km s}^{-1}$). The correlator settings and observing times are summarised in Table 1.

The data were initially reduced using the Starlink program ORAC-DR, however the broad wings of the outflow were within the baseline region determined by this routine. The data were therefore rebaselined and smoothed with a gaussian kernel to lower velocity resolution in order to reduce noise using python scripts. During the ^{13}CO and C^{18}O observations, one of the HARP-B detectors (H04) had a particularly bad baseline, so after examination these data were re-reduced with this detector excluded. All observations were then converted to the main beam temperature scale (T_{mb}).

3 DETERMINATION OF OUTFLOW PROPERTIES

Previous studies of outflows (e.g. Bally et al. 1999; Beuther et al. 2002c; Stojimirović et al. 2006) have tended to define global velocity windows, often by eye, to apply to all spectra containing outflow emission, or to a single spatially integrated spectrum. While this may work well for simple regions with only one outflow, using a single velocity window for all spectra across a region assumes that the cloud systematic velocity and line-width do not vary with position and that the outflow has a roughly similar velocity extent in all spectra. In the case of our observations this is not a safe assumption, as the systematic velocity and the full-width half-maximum (FWHM) both vary by $\sim 2 \text{ km s}^{-1}$ across the outflow region and the velocity extent varies strongly with

Table 1. Observational Setup

Transition	Rest frequency (GHz)	Bandwidth (MHz)	No. of channels	Vel. Resolution (km s ⁻¹)	Obs. Type	On source time (min)
CO (J=1–0)	345.80	250	4096	0.053	Raster	52
	345.80	1000	1024	0.847	Raster	52
¹³ CO (J=1–0)	330.59	250	4096	0.055	Raster	71
C ¹⁸ O (j=1–0)	329.33	250	4096	0.056	Raster	71
HCO ⁺ (J=4–3)	356.73	250	4096	0.051	Grid	10
	356.73	1000	1024	0.821	Grid	10
SiO (J=8–7)	347.33	250	4096	0.053	Grid	20
H ¹³ CO ⁺ (J=4–3)	347.00	250	4096	0.053	Grid	20

position. We therefore set out below the method and criteria we have used to determine the velocity window and mass individually for each spaxel within which emission is attributed to the outflow.

(i) Some ¹²CO spectra show additional cloud emission at different systematic velocities to the main feature associated with the outflow (e.g. see Figure 3). Gaussian fits were used to remove these, where possible, from the spectra before measurements of the outflow properties were performed. Strict acceptance criteria were used for the fit results so that the peak velocity and line-width did not vary too much from the expected values in order to ensure that these fits did not remove outflow emission.

(ii) The maximum temperatures of both the ¹²CO and ¹³CO spectra were measured using gaussian fits to the central cloud emission.

(iii) The excitation temperature (T_{ex}) was calculated for the spectrum, assuming that the ¹²CO emission is optically thick and that the gas along a given line of sight can be characterised by a single excitation temperature.

(iv) The ¹³CO optical depth (τ^{13}) was calculated, assuming that the ¹³CO emission is optically thin.

(v) The systematic velocity of the cloud for the spectrum was taken to be the velocity of the peak of the gaussian fit to the ¹³CO emission line, as the ¹³CO spectra do not include a significant contribution from the outflow.

(vi) The emission at velocities within 3σ of the peak of the gaussian fit to the ¹³CO spectrum was associated with the cloud, rather than the outflow, in the ¹²CO spectrum.

(vii) We estimate the ¹²CO to ¹³CO isotopic ratio as a function of velocity ($R_{12/13}(v)$) for the spectrum, using a quadratic fit to the velocity window identified as cloud emission, in order to account for optical depth effects in the ¹²CO spectrum. The maximum value of the ratio was limited to 62 (Langer & Penzias 1993), the assumed intrinsic ratio when both transitions are optically thin.

(viii) The ¹³CO column density per velocity channel ($N(^{13}\text{CO})(v)$) was calculated from the ¹²CO spectrum, using $R_{12/13}(v)$ and τ^{13} to account for optical depth effects.

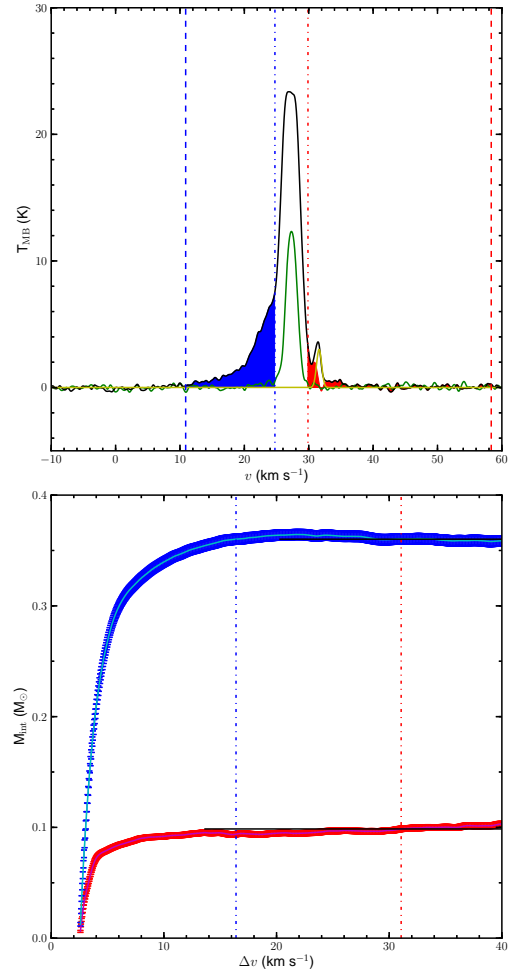


Figure 3. Top: Example ¹²CO (black) and ¹³CO (green) spectra. The yellow line indicates a gaussian fit to a non-outflow emission feature, which was removed when calculating the outflow properties. The inner and maximum outflow velocities are shown by the dashed and dash-dotted lines respectively, with the ¹²CO spectrum between these velocities shaded the appropriate outflow wing colour. Bottom: Cumulative integral of the mass in the outflow wings versus velocity offset for the spectrum shown above. The error bars indicate the random error associated with the cumulative integrated mass. The total integrated mass, obtained as discussed in section 3, step (xi) is indicated by the black line, while the velocity at which the cumulative integrated mass first becomes greater than or equal to the total mass, used as the maximum outflow velocity, is marked by the dot-dashed lines.

(ix) The mass per velocity channel ($m_{H_2}(v)$) was calculated from the ^{13}CO column density per velocity channel, assuming that the ratio of the H_2 column density to the ^{12}CO column density is 1.2×10^4 (Frerking, Langer & Wilson 1982), that the ratio of the ^{12}CO to ^{13}CO column density is 62 (Langer & Penzias 1993), that the mean molecular weight of the gas is 2.8 (Kauffmann et al. 2008), and using data with a pixel size of $7.3''$.

(x) The cumulative mass per velocity channel was calculated separately for the red and blue outflow lobes as a function of the velocity offset (Δv) from the systematic velocity of the cloud, starting at the inner outflow velocity defined in step (vi) and stopping at a velocity offset of 57.5 km s^{-1} , determined to be free of outflow emission in all spectra (see Figure 3 for an example).

(xi) We calculate the total integrated mass in the outflow lobe for the spectrum using a constant least-squares fit to the velocities larger than the point at which the ^{12}CO spectrum first becomes negative, i.e. has roughly reached the background level. The maximum velocity of the outflow lobe for the spectrum is then defined as the velocity at which the integrated mass first becomes greater than or equal to the total integrated mass (see Figure 3 for an example).

(xii) The momentum per velocity channel is calculated by multiplying the mass per velocity channel calculated in step (ix) by the velocity offset of each channel from the systematic cloud velocity and the kinetic energy per velocity channel by multiplying by half the velocity offset squared. The total momentum and kinetic energy in each lobe for the spectrum are then calculated as the integrals of the momentum and kinetic energy per velocity channel between the inner and maximum outflow velocities, as defined in steps (vi) and (xi).

While removing other cloud emission features in step (i) may have resulted in removal of a small amount of outflow emission, we consider such a conservative approach to be preferable to not removing this cloud emission. Examples of the regions where such emission has been identified for removal are indicated using yellow contours in the position-velocity plots in Figure 4, while the outflow velocity windows are shown using red and blue contours respectively. The equations used for steps (iii),(iv),(viii) and (ix) can be found in Wilson (2009).

While the random uncertainty in the mass due to thermal noise is relatively small (e.g. see the error bars in Figure 3), these are undoubtedly dominated by systematic errors. Buckle et al. (2009) estimate the systematic calibration errors for the JCMT to be $\sim 20\%$ and the various abundance ratios used are not particularly well known. In addition, the values used here were primarily measured in average ISM/molecular cloud conditions, so may not be representative of the abundance in star formation regions where depletion, photodissociation and fractionation processes can vary depending on position, species and even isotope. Masking within 3σ in step (vi) is reasonably conservative, as shown in Figure 4, and probably leads to some outflow emission at

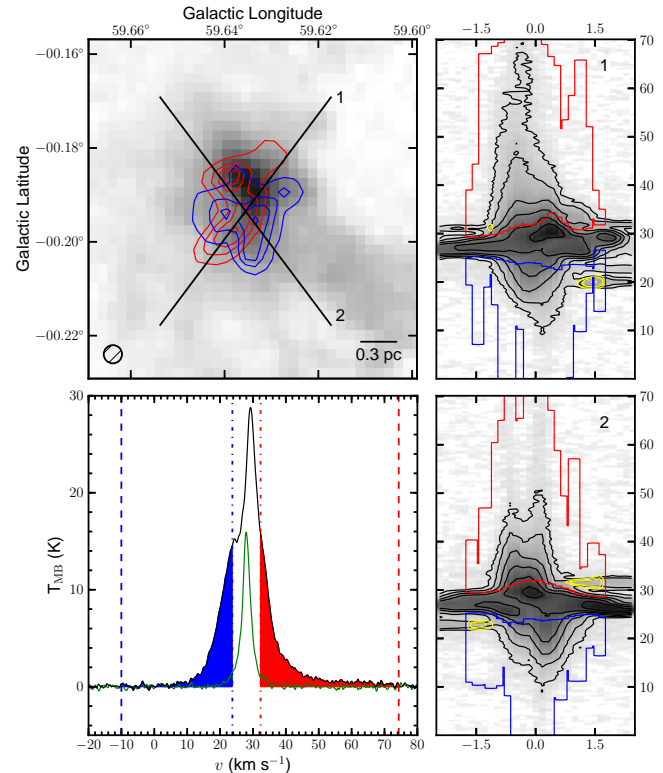


Figure 4. Outflows identified from HARP-B data. Top left: Integrated ^{13}CO emission shown in greyscale with red and blue contours showing outflow emission detected in ^{12}CO for the same region as in Figure 2. The red and blue contour levels are 25, 50, 75, 100 and 125 K km s^{-1} . Right, top and bottom: Position-velocity (PV) cuts through the ^{12}CO data, indicated by diagonal numbered lines in the top right plot, shown in a square-root scale to emphasise low-scale emission. The levels of the black contours to the ^{12}CO data are 0.8, 2.15, 5.6, 10.5, 17 and 25 km s^{-1} , while the yellow contours follow the same scale and indicate the regions of non-outflow emission removed using gaussian fits as discussed in the text. The red and blue contours indicate the red and blue outflow velocity windows. Bottom Left: Example ^{12}CO (black) and ^{13}CO (green) spectra for the pixel at the centre of the two PV cuts, with all lines and shaded regions having the same meaning as the top plot in Figure 3.

low velocity offsets being removed, perhaps resulting in as large as a factor of 3 underestimation of the outflow mass (Downes & Cabrit 2007). However, this approach is more accurate than either not correcting for ambient material, which can result in a significant overestimate, or attempting a more complex correction without sufficient information (Cabrit & Bertout 1990). Despite our conservative masking of the cloud emission, it is also possible that some of the emission considered as associated with the outflow is actually due to local turbulent material. While it is difficult to estimate a numerical error related to these factors, by using abundance ratios which are commonly used by other authors in the literature, we expect that we are not significantly more susceptible than other studies. The properties presented below are probably accurate to a factor of a few.

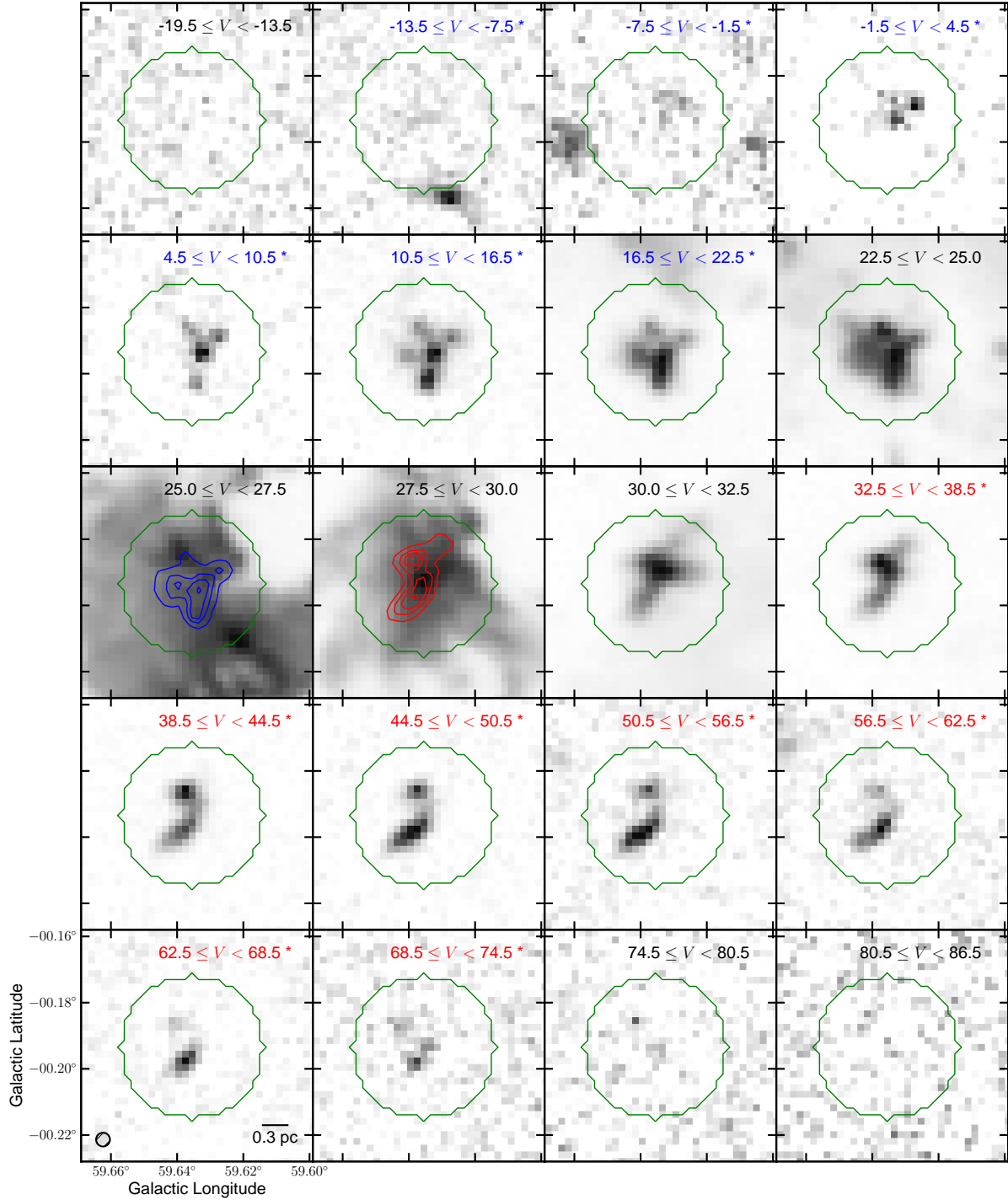


Figure 5. HARP-B ^{12}CO channel maps, integrated in 6 km s^{-1} slices except for the four slices at near the systematic velocity, which are 2.5 km s^{-1} in order to better reveal the exclusion of systematic emission from the outflow. The region to be considered when calculating the total mass in the region is indicated by the green contour, while the velocity integration of each slice is given in the top right corner of each plot. Those slices where at least 1% of the pixels lie within the outflow velocity window are denoted with a star and the text is colour-coded to the outflow wing. Contours of the total integrated emission in each outflow lobe are overlaid on the central velocity slices using the same contour levels as in Figure 3. The beam-size is shown in the bottom left of the plot.

4 RESULTS

4.1 Outflow properties

We performed the steps outlined in section 3 on all HARP ^{12}CO spectra within a spatial radius of 10 pixels ($\sim 0.81\text{pc}$) of the centre of the source, as this region encompasses the whole outflow. A series of channel maps with the channels identified as contributing to the outflow indicated are shown in Figure 5, with the region where our automated outflow identification was undertaken shown by the green contour.

It is clear from Figures 4 and 5 that the single outflow originally identified in the FCRAO ^{12}CO ($J=1-0$) data is at least partially resolved into multiple components at the resolution of the HARP-B observations. By examining both the channel and integrated maps, the blue wing emission breaks up into 4 or 5 components, while 3 or 4 separate components are visible in the red wing, though it is difficult to unambiguously identify the individual flows. In the following analysis, we tentatively identify four outflow components from the integrated emission maps in both the red and blue wings, as indicated in Figure 6, for which we have measured the mass, maximum relative velocity, momentum and kinetic energy, presented in Table 2. In regions of overlap, we assign spaxels in a mutually exclusive way. In order that our determination of individual flows does not overly affect our results, we also calculate the total properties of all the outflow emission. It is difficult to accurately estimate the angle of inclination between the line of sight and the outflow axis simply from our molecular observations, as the individual components are not well resolved or elongated, so we do not undertake an inclination correction for our velocities, momenta and energies. Thus the values of the quantities calculated below are lower limits to the true values and we are unable to calculate dynamical timescales.

4.2 The Ambient Molecular Cloud

The molecular clump associated with the outflow lies within a radius of $\sim 0.81\text{ pc}$ (10 pixel), shown by the green contour in Figure 5, and has a mass, measured from the ^{13}CO observations, of 3655 M_{\odot} , with 458 M_{\odot} in dense gas as measured using the HARP-B C^{18}O ($J=3-2$) data and a ratio of the C^{18}O and ^{12}CO column densities (i.e. $N(^{12}\text{CO}) / N(\text{C}^{18}\text{O})$) of 500 (Frerking, Langer & Wilson 1982). The same velocity window was used as for the outflow mass measurements, but without masking the line centre. Assuming that clump is spherical with a radius of 0.81 pc , we calculate its gravitational binding energy from the ^{13}CO mass to be 1.4×10^{48} ergs. We also calculate the turbulent energy (E_{turb}) of the clump using:

$$E_{\text{turb}} = (3/16 \ln 2) M_{\text{cloud}} \Delta V_{\text{FWHM}}^2 \quad (1)$$

from Arce & Goodman (2001) to be 1.7×10^{47} ergs, where V_{FWHM} is the average ^{13}CO FWHM of 2.4 km s^{-1} and M_{cloud} is the ^{13}CO clump mass. The combined energy of the outflow, even without inclination correction, is therefore approximately enough to drive the turbulence in the clump, and would provide enough energy to unbind the clump if $i \lesssim 15^\circ$.

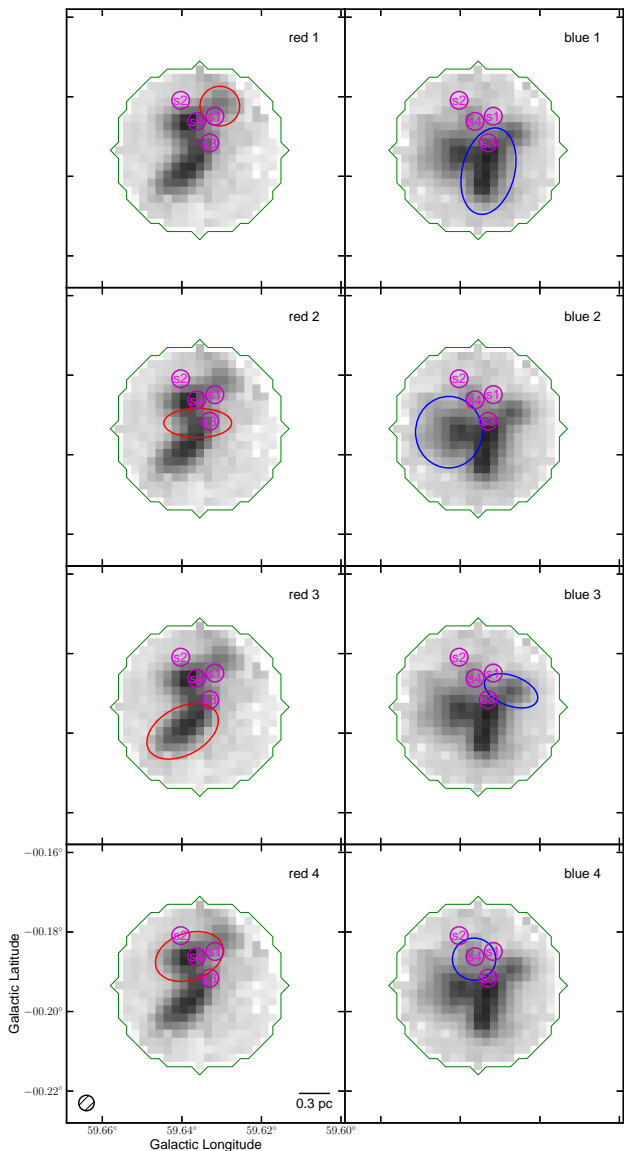


Figure 6. Red and blue outflow components indicated with coloured ellipses overlaid on the integrated ^{12}CO emission map corresponding to that line wing, as shown with contours in Figure 5. The numbers in the top right corner of each plot are the component numbers, also used in Table 2. The green contour is the same as in Figure 5. The four sources (s1-s4) associated with the clump containing the outflows are indicated in magenta. See sect. 4.3 for more details.

4.3 Associated YSOs

In order to explore the (proto)-stellar sources which are potentially associated with the detected outflows, we first note that four sources can be seen in Figure 2 which are probably associated with the molecular clump. Photometry data for these sources was gathered from the UKIDSS Galactic Plane Survey at J , H and K bands (Lucas et al. 2008), the GLIMPSE survey in the four Spitzer IRAC bands (Benjamin et al. 2003) and preliminary PACS $70\text{ }\mu\text{m}$ and $160\text{ }\mu\text{m}$ from the Hi-GAL survey (Molinari et al. 2010a; Elia et al. 2010). For the two sources not detected at all four IRAC bands, and for all sources from MIPS GAL $24\text{ }\mu\text{m}$

Table 2. Measured outflow properties

Component	M (M_{\odot})		Δv_{\max} (km s^{-1})		P ($M_{\odot} \text{ km s}^{-1}$)		E (10^{45} ergs)	
	r	b	r	b	r	b	r	b
1	8.5	30.3	38.6	38.9	48.9	196.3	3.29	15.93
2	9.7	26.0	50.5	41.6	74.9	142.1	8.94	9.50
3	18.7	5.8	48.5	42.6	173.3	44.8	28.13	4.51
4	22.9	6.9	46.9	37.4	175.7	52.9	19.02	4.90
total	59.8	69.1			472.9	436.1	59.38	34.84

Table 3. Properties derived from SED fitting

Source	$F_{bol}(10^{-12} \text{ W m}^{-2})$	$\log_{10}(L/L_{\odot})$
s1	3.2 ± 0.9	2.7 ± 0.2
s2	33.8 ± 14.4	3.8 ± 0.2
s3	50.8 ± 9.4	3.9 ± 0.2
s4	4.0 ± 0.7	2.8 ± 0.2
total	91.8 ± 17.2	4.2 ± 0.4

images (Carey et al. 2009) aperture fitting photometry was performed to obtain flux data as in Mottram et al. (2010). Sources 2 and 3 are mildly saturated in the $24 \mu\text{m}$ images, so the fluxes for these sources are treated as lower limits. In the Hi-GAL SPIRE $250 \mu\text{m}$, $350 \mu\text{m}$ and $500 \mu\text{m}$ images, the sources are too close together for reliable photometry to be obtained for the individual components. We therefore performed one aperture fitting photometry measurement encompassing all the sources, and use the flux obtained as an upper limit for sources 2,3 and 4. Source 1 is not included in this process because it is not detected at $160 \mu\text{m}$.

The spectral energy distributions (SEDs) of these sources were then fit using the model fitter of Robitaille et al. (2007) with similar input parameters to those used in Mottram et al. (2011b). We use a distance of $2.3 \pm 0.5 \text{ kpc}$ for all sources, where the distance error is set conservatively based on the difference between the photometric and kinematic distances rather than the error on the photometric distance from Massey, Johnson & Degioia-Eastwood (1995), which is much smaller. The SEDs and fits are shown in Figure 7, while the results are presented in Table 3.

Despite the increase in resolution between the FCRAO and HARP-B data, it is still not simple to associate the sources directly with individual outflow components. However, sources 1, 3 and 4 all seem spatially related to the observed outflows, particularly sources 3 and 4. Based on values given in Table 1 of Mottram et al. (2011a), the sources have luminosities consistent with spectral types in the mid to early B type, with the most massive (S3) being a B1–B0.5. The absence of detected radio continuum emission in Red MSX Source (RMS) Survey (Urquhart et al. 2008) VLA 5 GHz observations of this region (Urquhart et al. 2009) suggests that these sources are not powering HII regions, so have yet to reach the main sequence.

4.4 SiO, HCO^+ & H^{13}CO^+

The shock front and heating caused by molecular outflows interacting with surrounding cloud material strongly effects the chemistry of the surrounding region by releasing depleted molecules like SiO from grain mantles into the gas phase (e.g. Caselli, Hartquist & Havnes 1997; Schilke et al. 1997), increasing its relative abundance by factors of $\sim 10^2$ – 10^6 with respect to the ambient material (e.g. Martin-Pintado, Bachiller & Fuente 1992; Garay et al. 1998). Given that the depletion timescale for SiO onto dust grains is relatively short in normal molecular cloud conditions, of order 10^2 – 10^4 yrs (Mikami et al. 1992; Martin-Pintado, Bachiller & Fuente 1992), the presence of this molecule is therefore a good indicator that an outflow is currently active, rather than being a fossil flow. Our SiO observations are shown in Figure 8, where we detect broad emission ($\text{FWHM} \approx 20 \text{ km s}^{-1}$) towards the centre of the outflow, indicating that the outflows in this region are indeed active and not left over from previous activity. The amplitude observed is consistent with other observations (e.g. Klaassen & Wilson 2007). The H^{13}CO^+ observations have a line-centre of 27.8 km s^{-1} and a FWHM of 3.3 km s^{-1} , consistent with the C^{18}O lines for the same position, so the HCO^+ and H^{13}CO^+ emission is most likely associated with the core/envelope rather than the outflow. The $\text{HCO}^+/\text{H}^{13}\text{CO}^+$ ratio for this location is in the range 7–28, much lower than the expected abundance ratio for $^{12}\text{C}/^{13}\text{C}$ of 62 indicating that HCO^+ is optically thick and thus the double-peaked emission profile is almost certainly due to self-absorption.

5 DISCUSSION & CONCLUSIONS

The total mass within the outflow components, as obtained from the HARP-B ^{12}CO ($J=3-2$) observations is $129 M_{\odot}$, while the core mass derived from the BGPS 1.1mm dust continuum source is $327 \pm 112 M_{\odot}$. The mass in dense gas, as measured from C^{18}O ($J=3-2$) data is $458 M_{\odot}$, which agrees reasonably well with the core mass.

Using the BGPS core mass and the relationship between outflow and core mass obtained by Beuther et al. (2002c, their Fig 7.) to the Beuther et al. (2002b) sample results in an expected outflow mass of $\sim 10.3 M_{\odot}$, an order of magnitude smaller than detected. The outflow-to-core mass ratio is 0.4, higher than any of the sources reported by Beuther et al. (2002b,c), though the total luminosity of the associated YSOs is not particularly high compared to their

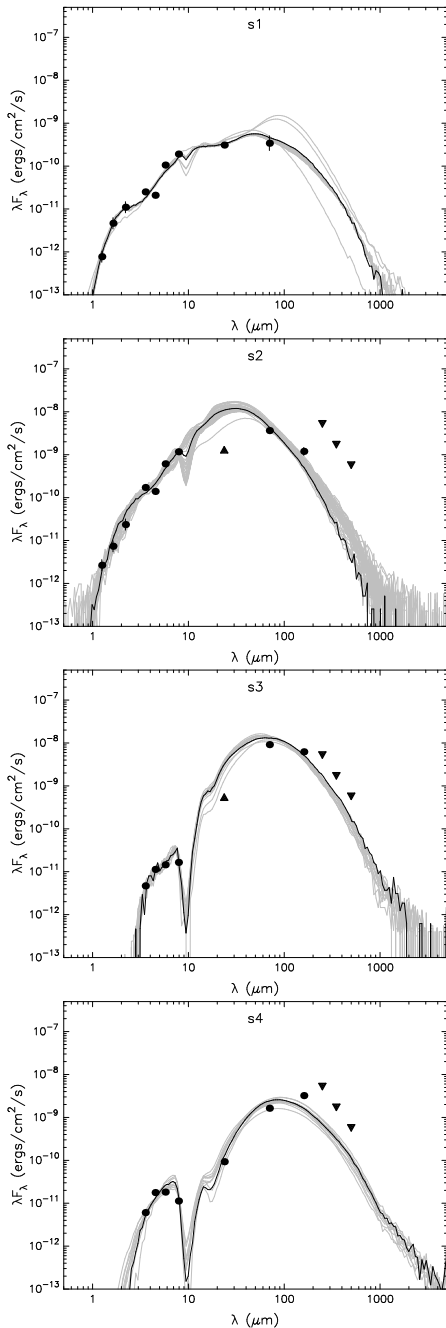


Figure 7. SEDs of the four YSOs associated with the outflow material, located as indicated in Figure 6. Detections are indicated with filled black circles while upper and lower limits are indicated with upwards and downwards pointing filled black triangles respectively. The best fit model is shown as a black line while all other fits within a given $\Delta\chi^2$ of the best fit are shown by grey lines.

sample. This suggests that these new outflows are either more efficient at entraining material or more energetic than those in the Beuther et al. (2002b) sample. If we assume an age for the outflows of 10^4 yrs (5×10^5 yrs), the mechanical luminosity of the combined outflows is $79L_{\odot}$ ($2L_{\odot}$), resulting in a ratio of the mechanical to YSO luminosity of 0.5% (0.01%). In order to compare with the results of Beuther et al. (2002c) we must first account for the increase

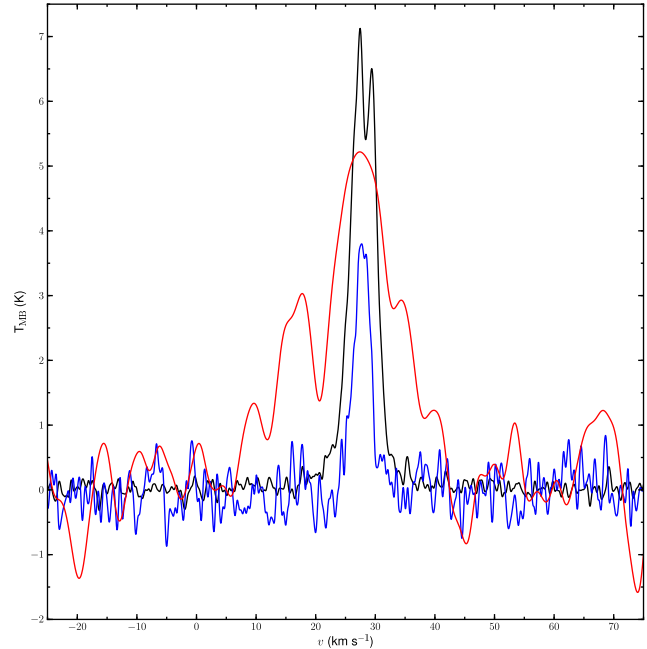


Figure 8. HCO^+ (black), H^{13}CO^+ (blue) and SiO (red) spectra smoothed to 0.5 km s^{-1} , 0.5 km s^{-1} and 2.5 km s^{-1} respectively for the central position of the outflow. The H^{13}CO^+ spectra have been multiplied by 5 and the SiO by a factor of 25 for improved visibility

which results from using the maximum outflow velocity and total mass rather than the channel velocity and mass when calculating the kinetic energy (approximately a factor of 25). Once this is taken into account, the highest mechanical to YSO luminosity ratio in their sample is 0.07% for IRAS 19410+2336 (G059.7833+00.0647 visible in the top left of Figure 1) and the median ratio is 0.002%.

There are several factors which could result in such high outflow-to-mass and mechanical-to-source luminosity ratios compared with previous studies. Firstly, it is possible that the additional driving source(s) for the outflows are heavily embedded within dense dust and gas core, though if this were the case it is surprising that there is not even a suggestion of this in Figure 2 as these data cover $3\text{--}250\mu\text{m}$. It could also be the case that despite our best efforts to be conservative, some cloud emission is still being included within the outflow velocity windows, but our mass measurements would have to drop by an order of magnitude to fall in line with other sources. The gas might have a higher than normal CO to H_2 ratio, leading to an overestimation of gas, though one has to ask why this particular region would be special in this regard.

Finally, it could be that outflow activity from young massive stars is variable due to variable accretion, in a similar way to the scenario suggested by Baraffe, Chabrier & Gallardo (2009, see also Baraffe & Chabrier 2010) for low-mass stars, where sources spend $\sim 1\%$ of their time in a high-accretion ($10^{-4}M_{\odot} \text{ yr}^{-1}$) phase and the rest accreting at a much lower rate ($10^{-6}M_{\odot} \text{ yr}^{-1}$). If the outflow from such a source was observed during or soon after the high accretion phase, a much higher mechanical luminosity would be observed

than after a long low-activity phase but the luminosity and core mass of the source would be similar.

In summary, we have confirmed an outflow with multiple components, probably associated with a group of four YSOs, in the Vulpecula Rift which has an outflow mass of $129 M_{\odot}$ and a core mass of $327 \pm 112 M_{\odot}$. The combined kinetic energy in the outflows (94×10^{45} ergs) is enough to drive turbulence in the local clump and potentially unbind the region, depending on inclination and the efficiency with which that energy is translated to the cloud. The outflows are not only energetic but also certainly active, due to the SiO detection, and thus presumably the related mid to early B type YSOs are currently still undergoing a phase of major accretion. Given the large reservoirs of cold dust detected in the sub-mm towards these sources, most likely associated with dense envelopes, this phase will probably continue for some time. The relatively red SEDs and the energetic nature of the outflows point to the relative youth of these sources, so it is likely these YSOs are destined to become more massive, rather than reach the main-sequence at their current mass.

Overall, some variation in outflow-to-core mass ratio is to be expected due to variations in cloud conditions, accretion rates, entrainment efficiency and the powering source. However, the outflow mass, momentum and energy must be in some way related to the mass and age of the central source, and thus the energy able to be injected, as found empirically by Beuther et al. (2002c). To find a young region where the outflows appear to be an order of magnitude more efficient than expected warrants further detailed investigation, in order to explore how outflows entrain mass from and impart energy and momentum to the surrounding molecular material. We therefore intend to undertake further interferometric observations at higher spatial resolution to study this region.

ACKNOWLEDGMENTS

The authors thank the anonymous referee for comments and suggestions which improved the clarity of the paper and Jennifer Hatchell for many helpful discussions during the course of this work. We are grateful to Michele Pestalozzi and Sergio Molinari for provision of improved Herschel Hi-GAL photometry and images. We also thank Ian Coulson and the staff of the JCMT for their assistance before and during our observations, and Thomas Robitaille and Eli Bressert for help with plotting using python. This work was supported by STFC Grant ST/F003277/1 to the University of Exeter. The JCMT is operated by The Joint Astronomy Centre on behalf of the Science and Technology Facilities Council of the United Kingdom, the Netherlands Organisation for Scientific Research, and the National Research Council of Canada. The Five College Radio Astronomy Observatory was supported by NSF grant AST 0838222.

REFERENCES

- Aguirre J. E. et al., 2011, *ApJS*, 192, 4
 Arce H. G., Borkin M. A., Goodman A. A., Pineda J. E., Halle M. W., 2010, *ApJ*, 715, 1170
 Arce H. G., Goodman A. A., 2001, *ApJ*, 554, 132
 Arce H. G., Shepherd D., Gueth F., Lee C., Bachiller R., Rosen A., Beuther H., 2007, *Protostars and Planets V*, 245
 Bally J., Reipurth B., Lada C. J., Billawala Y., 1999, *AJ*, 117, 410
 Banerjee R., Klessen R. S., Fendt C., 2007, *ApJ*, 668, 1028
 Baraffe I., Chabrier G., 2010, *A&A*, 521, A44+
 Baraffe I., Chabrier G., Gallardo J., 2009, *ApJL*, 702, L27
 Beichman C. A., Neugebauer G., Habing H. J., Clegg P. E., Chester T. J., eds., 1988, *Infrared astronomical satellite (IRAS) catalogs and atlases, Vol. 1: Explanatory supplement*
 Benjamin R. A. et al., 2003, *PASP*, 115, 953
 Beuther H., Schilke P., Gueth F., McCaughrean M., Andersen M., Sridharan T. K., Menten K. M., 2002a, *A&A*, 387, 931
 Beuther H., Schilke P., Menten K. M., Motte F., Sridharan T. K., Wyrowski F., 2002b, *ApJ*, 566, 945
 Beuther H., Schilke P., Sridharan T. K., Menten K. M., Walmsley C. M., Wyrowski F., 2002c, *A&A*, 383, 892
 Bica E., Bonatto C., Dutra C. M., 2008, *A&A*, 489, 1129
 Billot N., Noriega-Crespo A., Carey S., Guieu S., Shenoy S., Paladini R., Latter W., 2010, *ApJ*, 712, 797
 Billot N. et al., 2011, *ApJ*, 735, 28
 Brand J., Blitz L., 1993, *A&A*, 275, 67
 Brunt C. M., Heyer M. H., Mac Low M., 2009, *A&A*, 504, 883
 Buckle J. V. et al., 2009, *MNRAS*, 399, 1026
 Cabrit S., Bertout C., 1990, *ApJ*, 348, 530
 Carey S. J. et al., 2009, *PASP*, 121, 76
 Carroll J. J., Frank A., Blackman E. G., Cunningham A. J., Quillen A. C., 2009, *ApJ*, 695, 1376
 Caselli P., Hartquist T. W., Havnes O., 1997, *A&A*, 322, 296
 Chapin E. L. et al., 2008, *ApJ*, 681, 428
 Churchwell E., 1999, in *NATO ASIC Proc. 540: The Origin of Stars and Planetary Systems*, C. J. Lada & N. D. Kylafis, ed., p. 515
 Curtis E. I., Richer J. S., Swift J. J., Williams J. P., 2010, *MNRAS*, 408, 1516
 Downes T. P., Cabrit S., 2007, *A&A*, 471, 873
 Ehlerová S., Palouš J., Huchtmeier W. K., 2001, *A&A*, 374, 682
 Elia D. et al., 2010, *A&A*, 518, L97
 Frerking M. A., Langer W. D., Wilson R. W., 1982, *ApJ*, 262, 590
 Garay G., Köhnenkamp I., Bourke T. L., Rodríguez L. F., Lehtinen K. K., 1998, *ApJ*, 509, 768
 Hatchell J., Dunham M. M., 2009, *A&A*, 502, 139
 Kauffmann J., Bertoldi F., Bourke T. L., Evans, II N. J., Lee C. W., 2008, *A&A*, 487, 993
 Klaassen P. D., Wilson C. D., 2007, *ApJ*, 663, 1092
 Langer W. D., Penzias A. A., 1993, *ApJ*, 408, 539
 Lucas P. W. et al., 2008, *MNRAS*, 391, 136
 Martin-Pintado J., Bachiller R., Fuente A., 1992, *A&A*, 254, 315
 Massey P., Johnson K. E., Degioia-Eastwood K., 1995, *ApJ*, 454, 151
 Matzner C. D., 2007, *ApJ*, 659, 1394
 Matzner C. D., McKee C. F., 2000, *ApJ*, 545, 364

- Mikami H., Umemoto T., Yamamoto S., Saito S., 1992, ApJL, 392, L87
- Molinari S. et al., 2010a, A&A, 518, L100
- , 2010b, PASP, 122, 314
- Mottram J. C., Brunt C. M., 2010, Highlights of Astronomy, 15, 795
- Mottram J. C. et al., 2011a, ApJL, 730, L33
- Mottram J. C., Hoare M. G., Lumsden S. L., Oudmaijer R. D., Urquhart J. S., Meade M. R., Moore T. J. T., Stead J. J., 2010, A&A, 510, A89
- Mottram J. C. et al., 2011b, A&A, 525, A149
- Nakamura F., Li Z.-Y., 2007, ApJ, 662, 395
- Pascale E. et al., 2008, ApJ, 681, 400
- Pudritz R. E., Ouyed R., Fendt C., Brandenburg A., 2007, Protostars and Planets V, 277
- Richer J. S., Shepherd D. S., Cabrit S., Bachiller R., Churchwell E., 2000, Protostars and Planets IV, 867
- Robitaille T. P., Whitney B. A., Indebetouw R., Wood K., 2007, ApJS, 169, 328
- Rosolowsky E. et al., 2010, ApJS, 188, 123
- Russeil D. et al., 2011, A&A, 526, 151
- Schilke P., Walmsley C. M., Pineau des Forets G., Flower D. R., 1997, A&A, 321, 293
- Sharpless S., 1959, ApJS, 4, 257
- Sridharan T. K., Beuther H., Schilke P., Menten K. M., Wyrowski F., 2002, ApJ, 566, 931
- Stojimirović I., Narayanan G., Snell R. L., Bally J., 2006, ApJ, 649, 280
- Tomisaka K., 2000, ApJL, 528, L41
- Urquhart J. S., Hoare M. G., Lumsden S. L., Oudmaijer R. D., Moore T. J. T., 2008, in Astronomical Society of the Pacific Conference Series, Vol. 387, Massive Star Formation: Observations Confront Theory, H. Beuther, H. Linz, & T. Henning, ed., p. 381
- Urquhart J. S. et al., 2009, A&A, 501, 539
- Wilson T. L., 2009, ArXiv e-prints
- Yamada M., Machida M. N., Inutsuka S., Tomisaka K., 2009, ApJ, 703, 1141